ARTICLE

Experimental Studies on the Interactions between Au Nanoparticles and Amino Acids: Bio-Based Formation of Branched Linear Chains

Manish Sethi and Marc R. Knecht*

Department of Chemistry, University of Kentucky, 101 Chemistry—Physics Building, Lexington, Kentucky 40506-0055

ABSTRACT Biomacromolecules represent new structures employed for the fabrication, assembly, and subsequent use of nanomaterials for a variety of applications. By genetically selecting for the binding abilities of these bio-based molecules, the generation of materials with enhanced and environmentally sound properties is possible. Unfortunately, the level of understanding as to how the biomolecules bind and arrange on the nanomaterial surface is incomplete. Recent experimental and theoretical results suggest that the binding is dependent upon the peptide composition, sequence, and structure; however, these results were obtained for two-dimensional surfaces of the targeted inorganic material. Changing of the sample from two-dimensional targets to in solution three-dimensional nanomaterials presents a challenge because the level of analytical characterization for the latter system is minimal. Here we present our recent studies on the interactions between Au nanoparticles and the amino acid arginine. In our experimental design, the introduction of increasing concentrations of arginine to citrate-capped Au nanoparticles resulted in the formation of branched linear chains of the spherical nanomaterials. This assembly process was able to be monitored using UV—vis spectroscopy, transmission electron microscopy, and dynamic light scattering. The final results suggest that incomplete substitution of the original citrate surface passivant with the amino acid occurs, resulting in surface segregation of the two species. The segregation effect produces a dipole across the Au nanoparticle surface to drive the linear assembly of the materials in solution. Such results can possibly be exploited in understanding binding motifs and modes for biomolecules on the surface of functional nanomaterials.

KEYWORDS: bioinspired nanomaterials • biological—metal interfaces • Au nanoparticles • amino acids • nanomaterials assembly

INTRODUCTION

The fabrication and use of nanomaterials employing biologically relevant molecules has become a rapidly growing research area (1–3). These materials demonstrate unique properties that are directly employable for uses such as catalysts (4, 5) enzyme mimics (6), biological sensors (3, 7, 8), and biobatteries (9). While nature has already designed a series of materials that by themselves can find important applications, the number of natural materials available is limited. To overcome this drawback, phage display techniques have been developed to isolate short peptide sequences responsible for the fabrication of inorganic nanomaterials with different compositions, including ZnS (10), FePt (11), Ag (12), and Au (4, 12), as well as a variety of other compositions (2, 8, 13, 14). It is believed that the peptides are able to bind to the growing inorganic surface to prevent bulk aggregation, thus yielding peptide-stabilized nanoparticles in solution. While the peptides bind to the surface of the nanoparticle, it is clear that the inorganic components are solvent-accessible based upon known interactions with reagents in solution (4, 6). This suggests that the peptides are specifically arranged on the nanoparticle surface such that solvent exposure to the metallic component occurs in a controlled manner without resulting in nanoparticle agglomeration. Such interactions are desirable and can be exploited for a variety of nanomaterial applications, most notably catalytic and electronic reactivity. Unfortunately, little experimental information is known about the peptide/nanoparticle surface interface, which is critical to the subsequent design and activity of the material.

Recently, both experimental and theoretical evidence has become available to understand the process by which biomolecules bind to the surface of inorganic solids (15–22). Experimental studies are typically focused on surface adsorption isotherms or fluorescence-based quantitation of peptide binding using two-dimensional thin films of their specific target (15, 18, 20, 22). These valuable studies have demonstrated that amino acids, specific peptide sequences, and peptidyl geometric structures can directly affect biomolecular binding capabilities. In studies of Au and Pt binding peptides, constrained cyclic motifs possessed enhanced binding strengths as compared to their linear counterparts, which may arise from the inherent cell or phage-based selection processes as looped peptide conformations are occasionally employed for these combinatorial methods (15, 18). Computational techniques, such as density functional theory, have also been applied to ascertain the ad-

* To whom correspondence should be addressed. Phone: (859) 257-3789. E-mail: mrknec2@email.uky.edu.
Received for review March 10, 2009 and accepted May 5, 2009

DOI: 10.1021/am900157m

Published on Web 05/28/2009

sorption behavior of amino acids and peptides on metallic surfaces (16, 19). These studies have recognized different binding strengths for a variety of amino acids whose side chains possess inorganic binding moieties. For instance, Hong et al. have theoretically probed the binding abilities of arginine (Arg), lysine (Lys), and aspartic acid (Asp) to Au and Pd surfaces (16). In this study, Arg was able to weakly bind to a Au(111) surface via interactions with the guanidinium group of the side chain. These studies were again processed on simulated flat surfaces; however, experimentally addressing similar analyses on three-dimensional nanoparticle structures in solution remains challenging. Traditional experimental surface techniques such as quartz crystal microbalance and surface plasmon resonance are unable to address the in solution binding abilities of these peptides and their constituent amino acids for a particular nanoparticle surface. Such studies are critical to addressing the surface ligand structural characteristics and arrangements of these materials and the experimental binding strengths, as well as for use in the design of multicomponent, bioinspired structures where surface interactions are critical to their fabrication and assembly.

In separate studies, information concerning the ligand arrangement on Au nanoparticle surfaces has begun to be intensively studied (23–28). Using traditional thiol-based molecules, "rippled" ligand surfaces have been observed on Au nanoparticles possessing a mixed monolayer of two species (23, 25, 26). The driving force for this to occur is based upon thermodynamic considerations (26), thus resulting in controlled surface segregation of the ligands. As a result, electronic dipoles, as well as patchy, electronically charged networks, can be generated along the particle surface (23, 25). Au nanoparticle stability is achieved via surface electrostatic repulsion effects (28), which can be drastically altered on individual nanoparticles using selected ligand-exchange methods (28, 30, 31). As a result of the patchy electronic surface, assembly of the nanoparticles in solution can occur along the dipole moment, thus generating chainlike arrangements of nanoparticles that can be monitored using readily addressable solution and solid-state techniques (28, 30).

In this study, we present direct experimental evidence concerning the interactions and surface segregation of the amino acid Arg with Au nanoparticles in solution, as is shown in Scheme 1. This system was selected because the Arg side chain has been implicated as possessing binding capabilities to inorganic substrates (16) and has been observed in many material binding peptides, especially those isolated for Au surfaces (9, 15, 22, 32). To study this process, various concentrations of the amino acid were added to aqueous solutions of citrate-capped 15 nm Au nanoparticles, which resulted in the self-assembly of the nanomaterials to form long, branching linear chains in solution. Evidence attained by UV–vis spectroscopy, transmission electron microscopy (TEM), and dynamic light scattering (DLS) indicates that the Arg partially replaces the citrate stabilizer, thus resulting in a mixed monolayer. The organized nanoparticle

Scheme 1. Representative Scheme for the Formation of Linear Au Nanoparticle Assemblies Mediated by Arg

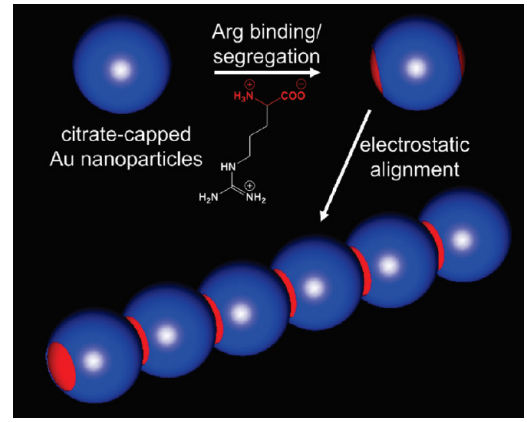

assembly process suggests that the Arg molecules self-segregate on the Au surface, resulting in negatively charged regions arising from the citrate molecules coexisting with neutral surface regions based upon the solvent-exposed, zwitterionic head groups of the amino acids. In response to the patchwork surface charge and the resultant nanoparticle dipole, the formation of linear nanoparticle chains occurs by allowing nanoparticles to collide and interact at the neutral regions. This process is accelerated when higher Arg concentrations are present, which can result in nanoparticle degradation at extremely high Arg concentrations. These results are important for three key reasons. First, the results suggest specific binding modes and motifs based upon amino acids and their interactions, which may translate to similar arrangements for metal binding peptides to explain metallic solvent accessibility. Second, this study provides a direct route for experimental evidence on the surface interactions between biomolecules and three-dimensional nanomaterials in solution, which is typically difficult to attain. Third, this method also represents a unique strategy to biologically control the fabrication of linear assemblies of nanoparticles that are challenging to organize because of the high degree of symmetry from the spherical species (33). Such arrangements may prove useful for electronic and optical applications.

EXPERIMENTAL SECTION

Chemicals. $HAuCl_4 \cdot 3H_2O$, L-arginine, and sodium citrate tribasic dihydrate were purchased from Sigma-Aldrich (St. Louis, MO). All chemicals were used as received. Milli-Q water (18 MΩ cm; Millipore, Bedford, MA) was used throughout.

Preparation of Citrate-Capped Au Nanoparticles. Au nanoparticles were prepared by the citrate reduction method (34). Before the reaction, all glassware was washed using aqua regia (3:1 HCl/HNO_3) and then rinsed with deionized water. For the reaction, a 50 mL aqueous solution of 1.00 mM $HAuCl_4$ was refluxed while stirring. Once solution refluxing was achieved, 5.00 mL of an aqueous 38.8 mM sodium citrate solution was added. Immediately, the solution changed from yellow to colorless. The reaction was refluxed for 15.0 min, and a final solution color of wine red was achieved. After the reaction, the solution was allowed to cool to room temperature prior to being filtered using a 0.45 μm filter. Before each analysis, the Au

nanoparticle samples were centrifuged at 5000 rpm for 2.00 min, from which the supernatant was studied.

Arg-Based Assembly of Citrate-Capped Au Nanoparticles. For this analysis, the Au nanoparticles were diluted to a concentration of 4.00 nM using Beer's law ($\epsilon = 3.6 \times 10^8$ cm^{-1} M^{-1}) (34). A total of 1.5 mL of the stock nanoparticle solution was then added to a standard 1.0 cm quartz cuvette. To each cuvette were added various concentrations of Arg from a 400 μM aqueous solution, resulting in final Arg reaction concentrations of 0, 20, 40, 80, 120, 160, and 200 μM. These concentrations were selected because they represented 0-, 1.0×10^4-, 2.0×10^4-, 4.0×10^4-, 6.0×10^4-, 8.0×10^4-, and 1.0×10^5-fold excesses of Arg as compared to the Au nanoparticles in solution, respectively. These samples are designated as 0, 10K, 20K, 40K, 60K, 80K, and 100K throughout the text. The final reaction volume was 3.0 mL for each sample; therefore, the final Au nanoparticle concentration was 2.00 nM. The reaction was allowed to proceed for 6.00 h, while being monitored using UV–vis spectroscopy.

Characterization. Time-resolved UV–vis spectra were obtained using an Agilent 8453 UV–vis spectrometer employing a 1.00-cm-path-length quartz cuvette (Starna). All spectra were background-subtracted against deionized water, which is the reaction solvent. Over a period of 6.00 h, spectra were recorded at 10.0 min intervals. TEM images of the assembly process were obtained using a JEOL 2010F transmission electron microscope operating at 200 keV, with a point-to-point resolution of 0.19 nm. A total of 5.00 μL of the reaction solution was pipetted onto the surface of a 400 mesh Cu grid coated in a thin layer of carbon (EM Sciences) and allowed to dry in a desiccator. DLS analyses were conducted on a Zetasizer Nano ZS System (Malvern Inc.) at 1.00 h intervals over a total time of 6.00 h.

RESULTS AND DISCUSSION

Au nanoparticles with an average diameter of 15 nm were synthesized using the citrate reduction method (34) and confirmed using UV–vis and TEM analyses (Figure S1 in the Supporting Information). The particles possessed the expected plasmon resonance peak at 520 nm, which was used to dilute the nanoparticles to a concentration of 4.00 nM using the Beer–Lambert law. To 1.50 mL of the nanoparticles were added various concentrations of Arg, resulting in a 0-, 10K-, 20K-, 40K-, 60K-, 80K-, or 100K-fold excess of the amino acid with respect to the nanoparticles to achieve a final solution volume of 3.00 mL, as discussed in the Experimental Section. This notation is subsequently used throughout the text to differentiate samples. The reactions were agitated initially and studied over a time period of 6.00 h to monitor changes in the nanoparticle stability. Arg was initially selected based upon its known affinity for Au surfaces and its frequency in many material binding peptides (15, 16, 32).

Figure 1 displays images of the reaction between the Au nanoparticles and Arg as they progressed over time, demonstrating a distinct color change. Prior to addition of the amino acid, the solution for each reaction was the expected red color. Immediately after Arg addition (Figure 1a), this red color is maintained for most samples; however, the 80K materials demonstrated a change to a deeper red color, and the 100K solution appeared purple. After 1.00 h of reaction time (Figure 1b), the 80K and 100K solutions are distinctly blue and the 60K reaction has become purple. For 0 and 20K, the original red color is observed, while the 40K

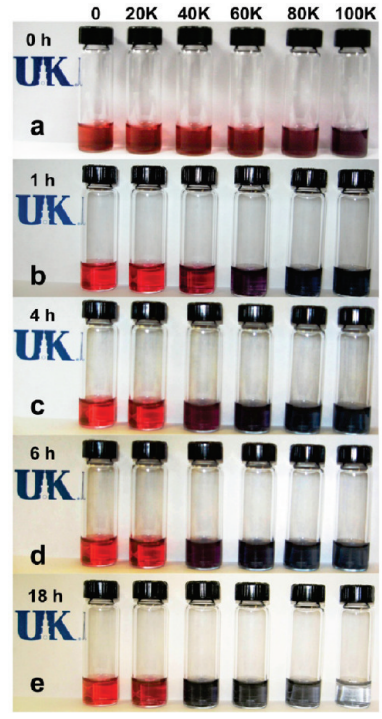

FIGURE 1. Photographs of the effect of Arg on Au nanoparticles at time intervals of (a) 0.00 h, (b) 1.00 h, (c) 4.00 h, (d) 6.00 h, and (e) 18.0 h.

solution becomes darker red. The changes in color progressed after 4.00 h, as shown in Figure 1c, to where the 60K solution is now deeper purple and is approaching a blue color, while the 40K sample is purple. At this time point, the 0 and 20K samples have remained red and the 80K and 100K samples remained blue. The solution colors observed at 4.00 h visually remained constant after 6.00 h of reaction time (Figure 1d); however, a dramatic change is observed after 18.0 h, as shown in Figure 1e. While the control sample, 0, has maintained the initial cherry red color, the 20K sample has evolved to a deeper red. The 40K sample has become deep blue as compared to the previous time point, and samples with higher Arg concentrations display a dimming of the solution color intensity. Even as the resultant blue color is maintained for the 60K and 80K sample, it has become distinctly lighter in intensity as compared to the 6.00 h time point. A more dramatic effect was also noted for the 100K sample. For these materials, a blue/black precipitate is observed at the bottom of the vial, in combination with a pale-blue solution.

Such visual observations of color changes are consistent with the aggregation of the Au nanoparticles in solution (3, 8, 29). The distinct color changes from red to purple to blue and precipitation of the 100K sample are anticipated for changes in the particle size from individual particles to larger aggregates. The color stability of the control sample suggests that the changes observed are directly associated with the Arg molecules in solution. Additionally, the noted differences in the rate of color change between the samples, from 20K to 100K, indicate that the nanoparticle aggregation is dependent upon the solution concentration of Arg, with faster rates arising for higher Arg concentrations. While

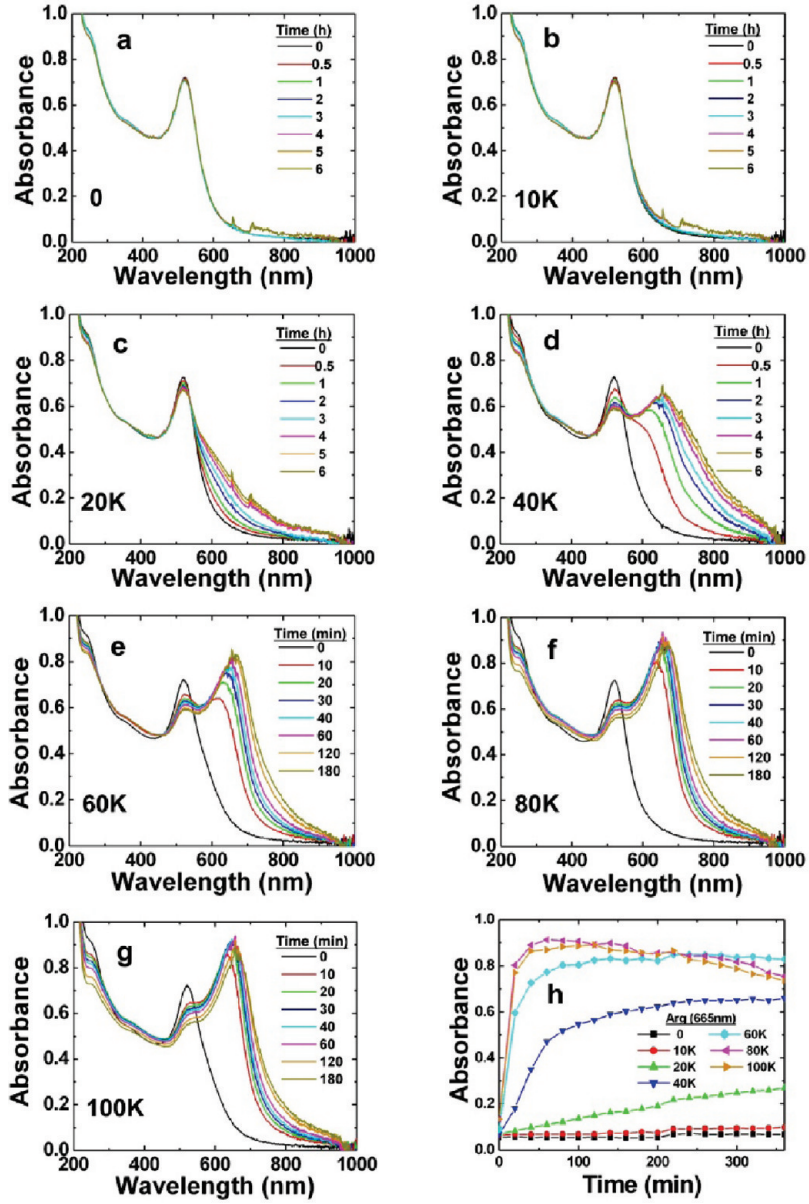

FIGURE 2. UV−vis analysis of the effects of Arg on Au nanoparticles for samples (a) 0, (b) 10K, (c) 20K, (d) 40K, (e) 60K, (f) 80K, and (g) 100K. (h) Time evolution for the production of the peak at 665 nm for all Arg concentrations studied.

these results suggest Arg-based aggregation, more quantitative analyses are required to determine the effects of the amino acid.

The aggregation process was initially analyzed using UV−vis spectroscopy. Such a technique is highly accurate in determining the assembly state of the material by shifts in their absorbance (3, 21, 36, 37). Figure 2 shows the spectral changes of the Au nanoparticles in response to Arg addition. Figure 2a specifically demonstrates that no change is observed in the spectrum of the Au nanoparticles over a period of 6.00 h in the absence of Arg. Additionally, at the lowest concentration of Arg studied, 10K (Figure 2b), no spectral shifts or secondary absorbance peaks are observed. As the Arg concentration is increased to 40.0 μM in the 20K sample (Figure 2c), definitive spectral changes are evident. Over a period of 6.00 h, the plasmon resonance peak at 520 nm of the individual Au nanoparticles decreases in intensity as a new absorbance centered at 665 nm increases. In this sample, no distinct peak is observed; however, the absorbance at higher wavelengths continually increases in a linear fashion. More distinctive changes are observed in the 40K sample, as shown in Figure 2d. For this sample, a well-resolved peak at 665 nm is developed as the initial 520 nm plasmon resonance decreases in intensity. This distinct peak is initially slightly broader than the original plasmon resonance yet is easily resolved over the 6.00 h time scale. For samples of higher Arg concentrations (60K, 80K, and 100K), the rate of peak formation increases dramatically; therefore, shorter time frames for the UV−vis analysis are presented to show their evolved changes over time. For the 60K sample shown in Figure 2e, the development of a strong and narrow absorbance at 665 nm is complete within 2.00 h. After this time point, no changes in the spectra are observed and both the 520 and 665 nm peaks remain constant. For the 80K

and 100K samples (parts f and g of Figures 2, respectively), results very similar to those of the 60K sample are observed, except faster rates of spectral change are noted. For both samples, growth of the 665 nm absorbance is terminated after 20.0 min, from which both peaks remain constant for ~40.0 min (1.00 h after reaction initiation). After this time point, the spectra demonstrate a progressive red shift and a decrease in intensity for the 665 nm peak, indicating a change in particle morphology at longer assembly durations. This change is accompanied by material precipitation at time points greater than 6.00 h; however, larger uncontrolled species are likely to exist in solution prior to this point (vide infra).

Figure 2h presents the growth of the 665 nm peak over the specified reaction time for all of the samples studied at the various Arg concentrations. It is evident that the growth rate of the new peak directly depends on the Arg concentration. For those samples with no spectral changes, 0 and 10K, no change in the absorbance at 665 nm is observed. For the 20K sample, a slow but consistent linear growth of the 665 nm absorbance is observed over 6.00 h. Note that for this sample only a rising broad absorbance at higher wavelength was observed and not a defined peak. Analysis of the 40K sample shows an initial increase in the absorbance at 665 nm, which eventually slows after 100 min post Arg addition. At this point, the growth rate decreases considerably; however, the intensity continues to increase over time. The 60K sample demonstrates a very fast growth rate, which plateaus after 1.00 h. After this rapid initial growth, the 665 nm absorbance remains constant, with no spectral changes observed for this sample. Similar results were obtained for both the 80K and 100K samples with fast absorbance intensity growth; however, this initial period was followed by a slow decrease in intensity over time. This diminishing factor is attributed to precipitation of the materials as the reaction progressed. Indeed, precipitation is observed for both samples, as shown in the image of Figure 1e. Interestingly, for all samples that displayed changes to their UV–vis spectra over time, while the initial 520 nm peak does decrease in intensity, its position remains constant over the entire analysis. Even when saturation of the peak at 665 nm is observed, suggestive of the termination of materials assembly, the 520 nm peak persists. As discussed below, this is likely due to the controlled aggregation process mediated by the Arg in solution.

While UV–vis analysis is commonly accepted to be sensitive to the aggregation/assembly state of the materials in solution, it is unable to discern the aggregate size or structural changes to the growing framework. To address any size changes in solution, whereby alleviating any possible drying effects, DLS analysis of the materials was conducted. These results are presented in Figure 3a, for all samples, with Figure 3b showing an expanded analysis for those materials studied with Arg concentrations below the 100K sample. For the 0 and 20K sample, black and red plots, respectively, no changes in the material size is observed after 6.00 h. The sample sizes remain constant around 20 nm,

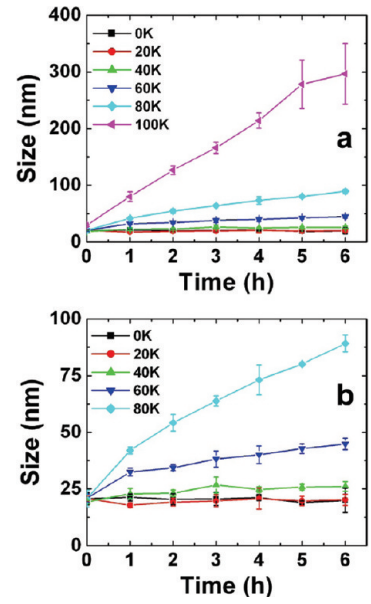

FIGURE 3. (a) DLS analysis of Au nanoparticles in the presence of Arg over a time period of 6.00 h. (b) Analysis for all samples with Arg concentrations less than that used in the 100K sample.

which is consistent with the hydrodynamic radius of the individual Au nanoparticles and the lack of or slow spectroscopically observed changes (38). For the 40K sample, green plot, a linear increase from an initial size of 19.1 nm to a size of 26.1 nm is achieved. At all time points, this sample possesses larger average aggregate sizes, as compared to samples with lower Arg concentrations, suggesting that a noticeable size shift is observed. At higher Arg concentrations, clear and linear size dependences are noted. For the 60K sample, plotted in royal blue, an increase in size is observed, which reaches an aggregate size of 44.8 nm after 6.00 h. This increasing trend is conserved for higher concentrations; however, faster rates of production of larger aggregates are observed for these materials. For the 80K sample, light-blue plot, this consistent growth process is maintained and terminates in an aggregate size of 89.2 nm at the 6.00 h time point. Finally, analysis of the 100K growth process, plotted in pink, demonstrates the fastest rate for all of the materials studied. As a result, generation of a final aggregate size of 297 nm occurs in 6.00 h, which is considerably larger in size than all other aggregated species studied.

While the DLS results indicate that assembly of the materials is occurring in solution, it is unable to determine if this process produces controlled final structures from the individual nanoparticle components. TEM analysis of the materials was thus conducted to ascertain the assembly state of the nanoparticles in response to Arg. On the basis of the above UV–vis results, which demonstrated a splitting of the plasmon resonance, a directed assembly mechanism appears to be mediating the process, which could result in a patterned nanoparticle structure. TEM grids were prepared 6.00 h post Arg addition for each sample from 0 to 100K, from which the images attained from these samples are presented in Figure 4. As expected, no assembly was observed for the 0 sample prepared in the absence of Arg, displayed in Figure 4a. Under these conditions, the Au nanoparticles remain inde-

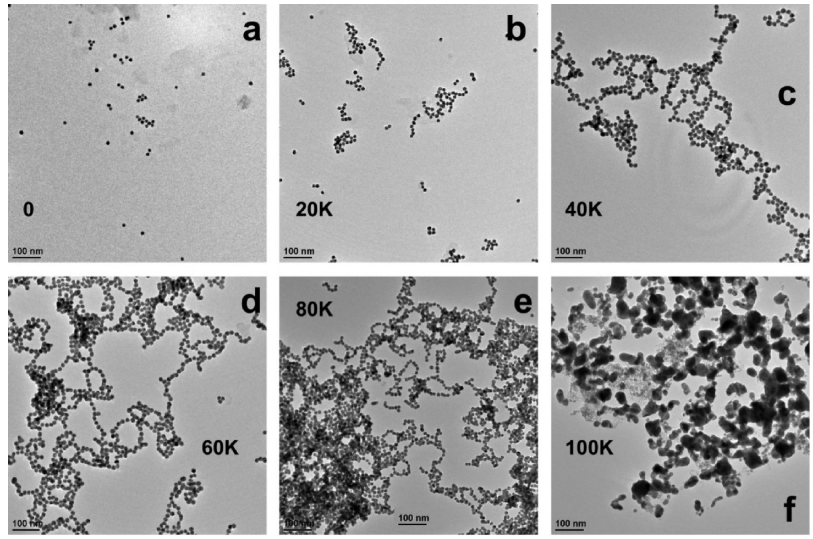

FIGURE 4. TEM micrographs of the Au nanostructures produced after 6.00 h of incubation with Arg for samples (a) 0, (b) 20K, (c) 40K, (d) 60K, (e) 80K, and (f) 100K.

pendent and highly dispersed upon the carbon grid surface. Similarly, for the 20K sample shown in Figure 4b, only small aggregated structures of the Au nanoparticles are observed. Surprisingly, short linear chains of Au nanoparticles were the dominant species observed for this sample. Approximately 3−10 nanoparticles could be seen in a linear arrangement, from which occasional chain clustering was also observed. In addition to these structures, an extensive number of independent and unassembled nanoparticles were also detected in this sample. Further analysis of the 40K sample (Figure 4c) demonstrated a higher degree of linear arrangement of Au nanoparticles. While long chains of the Au nanoparticles existed, branching points were apparent, which resulted in a networklike organization of the linear chains into a superstructure. This larger structure could stretch to >1.00 μm in dimension. TEM imaging of the 60K sample, displayed in Figure 4d, indicated that this linear branching trend continued for higher concentrations of Arg. In this sample, larger controlled aggregated networks were apparent. This trend of increased aggregation continued for higher Arg concentrations, with a noticeably denser network prepared for the 80K sample. In this sample, presented in Figure 4e, while linear chains were observed at the 6.00 h time point, large regions of the sample were observed to be in a more uncontrolled aggregated structure of variable size. This mixed type of aggregation is apparent in the TEM image where the linear chains are observed at the center of the image, while large uncontrolled aggregates are observed to surround the chains. Finally, only bulk, irregular Au structures were observed for the 100K sample 6.00 h post Arg addition (Figure 4f). No specific arrangement of these uncontrolled structures was discernable, with only random orientations observed for this sample.

While it appears to be evident that the Au nanoparticles indeed assemble in an organized linear manner in the presence of Arg, both the UV−vis and DLS data suggest that this process occurs over time rather than in a single immediate step. To analyze this process, TEM images were acquired for each sample at 1.00 h time points during the 6.00 h reaction time. The images attained for the 40K sample are presented in Figure 5, while the images for all other samples are included in Figures S2−S6 in the Supporting Information. Note that, for the 40K sample, a solution color change from red to purple was observed over this time period, in addition to the formation of a distinct secondary assembled absorbance peak at 665 nm in the UV−vis analysis. Prior to Arg addition (Figure 5a), no assembly of the materials is observed; however, after 1.00 h in the presence of Arg, small linear aggregates are noted (Figure 5b). These aggregates are well dispersed on the grid surface, intermixed with individual Au nanoparticles, indicating that not all of the materials are assembled. As the time progressed to 2.00 h in the presence of Arg, longer linear structures were observed, with a larger degree of branching as compared to the 1.00 h time point, as shown in Figure 5c. Further analysis at 3.00 h (Figure 5d) displays the formation of larger aggregated structures where the development of a network arrangement of nanoparticles occurs. Linear regions of Au nanoparticles remain; however, it appears as if branching regions collide to form interconnects between the two chains. This growth process progresses for the 4.00 and 5.00 h time points (parts e and f of Figure 5, respectively), where the networks continue to expand and become intermingled. Clear linear portions remain where longitudinal growth can ensue, yet other regions of more densely packed materials coexist. Finally, at a time point of 6.00 h (Figure 5g), large extended networks of the branched, linearly arranged Au nanoparticles exist. The linear portions persist; however, these chains are branched and interconnected at distinct points to form a highly integrated network of assembled Au nanoparticles. This imaging analysis appears to concur with the previous spectroscopic and scattering data, suggesting a dynamic growth process occurring over time.

It is worth noting that we attempted to analyze these images to attain statistical information on the assemblies. We have already addressed the aggregate size in solution

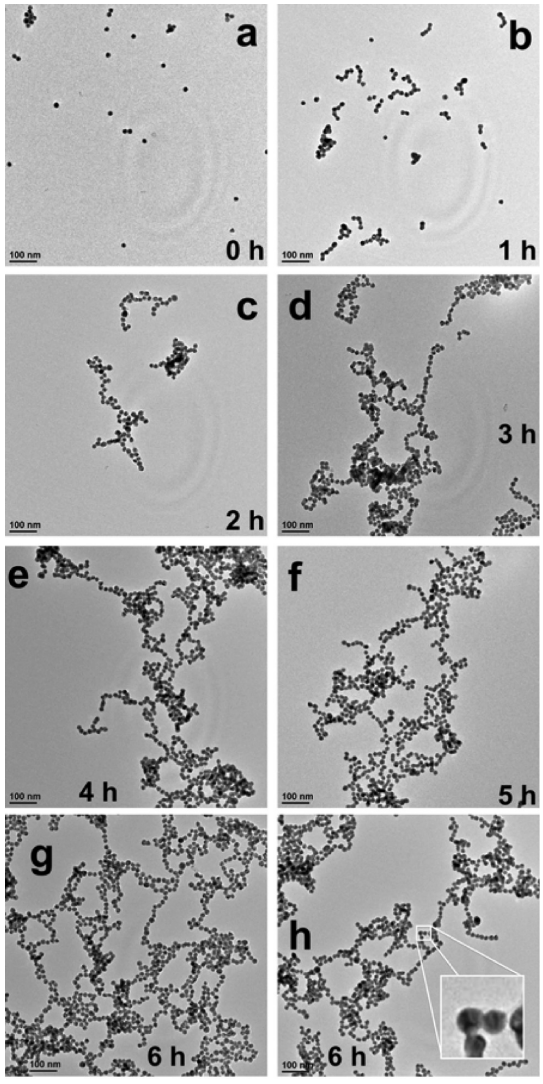

FIGURE 5. TEM analysis of the 40K Arg assembly process at time points of (a) 0.00 h, (b) 1.00 h, (c) 2.00 h, (d) 3.00 h, (e) 4.00 h, (f) 5.00 h, and (g) 6.00 h. (h) Linear network observed at 6.00 h, with the inset showing the fused necks between three Au nanoparticles.

via DLS studies, which can be complicated by the aggregate architectures and solution index of refraction, but attaining information on the number of particles per chain can be difficult. While such results for the 40K sample at the shorter time points (≤2.00 h) are possible, determining this value for the chained networks at longer times is challenging. For instance, at the 6.00 h time point of Figure 5g, neither a clear starting point nor a clear end point for the branched chain is able to be observed without a region from which the structure progresses. Indeed, certain parts of the chain do terminate throughout the structure; however, because of the bifurcated nature of the assembly, progression of the chain length can occur in other directions. As such, determining an exact number of nanoparticles per chain for such samples is complicated to impossible. While other considerations such as shape and solvent effects do factor into the DLS analysis, these results are consistent with changes in the solution color, UV−vis spectroscopic shifts, and the TEM-determined degree of assembly over time for all samples.

The observed nanoparticle assembly process, mediated by Arg in solution, is based upon the fundamental interactions between the nanoparticles and the amino acid molecules, which includes the binding strength of Arg to Au (16). This oriented assembly is likely to be driven by the formation of a patchy, segregated mixed monolayer on the surface of the Au nanoparticles (23, 28, 30), as presented in Scheme 1. This mixed surface is generated by incomplete ligand exchange of the initial negatively charged citrate surface passivant with the Arg. On the basis of theoretical modeling, Arg binds to the surface of the Au nanoparticle via the guanidinium group of the side chain (16). As a result, the zwitterionic head group is displayed to solution, which can drastically change the electronic nature of the nanoparticle surface. The pH value of our reaction is 7.02 after Arg addition; therefore, nearly all of the amino acid head groups are electronically neutral. Such changes to this layer are known to cause nanoparticle instability and lead to aggregation in solution by a minimization of the electrostatic repulsion between colloids (28, 30, 39, 40).

The formation of linear chains, rather than generation of a massive uncontrolled aggregate, is caused by the surface segregation of the two ligands on the nanoparticle. Such segregated patchy networks have previously been identified and studied using high-resolution STM analysis of Au-monolayer-protected clusters (24–27). In the present study, the segregation is driven by the electronic characteristics of the two surface ligands, citrate and Arg. It is known that zwitterionic species are able to form electrostatic networks when positioned in close proximity on three-dimensional surfaces (21, 41–43). These regions are stabilized and promoted by the electrostatic network of interactions formed between the multiple cationic amines and anionic carboxylic acids placed in close proximity, thus resulting in Arg surface segregation on the Au nanoparticles. Discharge of the network, either by charge changes or shielding, can liberate the surface-bound species (21); however, under the present conditions, only the zwitterions are present. As such, the driving force to form this surface electrostatic network results in partitioning of the amino acids from the remaining citrate stabilizers, when a mixed monolayer is present, producing an anisotropic surface containing both neutral and negatively charged regions. As a result of this effect, an electronic dipole across the particle is generated, upon which the linear arrangement of these species can occur. In addition, branching is anticipated because multiple neutral regions are possible, thus resulting in a focal point for chain splitting from individual nanoparticles.

TEM evidence supports this dipole-based alignment mechanism through the specific interactions that occur between two nanoparticles of the linear chain. As shown in Figure 5h, a linear network of Au nanoparticles is studied using the 40K system after 6.00 h. In the inset of a region of the nanoparticle superstructure, three Au nanoparticles are presented in which necking is observed between each of the three components. This necking process is initiated by the close proximity between the nanoparticles that is

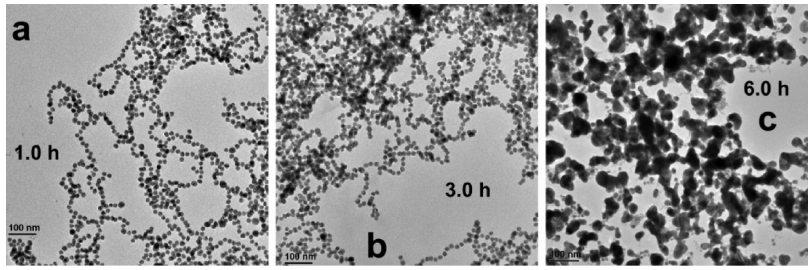

FIGURE 6. TEM micrographs of the 100K sample after (a) 1.00 h, (b) 3.00 h, and (c) 6.00 h. The degree of bulk formation increases as the reaction time progresses.

achieved by the dipole-based alignment over the electronically neutral regions of the nanoparticle surface. For this to occur, the distance between nanoparticles must be significantly minimized, which arises from a decrease in the electrostatic repulsion forces over these specific regions. These regions of low electrostatic repulsion are directly attributable to the patchy neutral regions of the amino acids on the nanoparticles. Furthermore, these fused nanoparticles suggest that alignment occurs in solution to facilitate the necking process, as such actions are unlikely to proceed in the solid state. This dipole-based process is likely to be influence by the solution conditions such that charge shielding can affect the assembly rate and/or length of chains produced. Indeed, when the solution dielectric is decreased by the addition of increasing volumes of DMSO (Figure S7 in the Supporting Information), the rate of assembly increases dramatically for the 40K sample.

Further evidence to support that the directed linear assembly occurs in solution, rather than from solvent evaporation during TEM sample preparation, arises from the UV−vis analysis. Prior to Arg addition, a single plasmon resonance is observed at 520 nm associated with the individual Au nanoparticles. As the ligand-exchange process ensues to form the nanoparticle dipoles and subsequent linear chains, a new absorbance peak develops at 665 nm with an isosbestic point at 550 nm. Such a growth process is consistent with the fabrication of one-dimensional nanostructures in which a large degree of anisotropy arises from the linear chains (21, 37, 39, 44–47). As a result of this structure, interparticle plasmonic coupling can occur along the chain axis; however, the secondary transverse direction, which is maintained as the diameter of the Au nanoparticles, remains constant. On the basis of this arrangement, two plasmon resonance peaks would be expected to arise from the two directions, with the 520 nm peak associated with the transverse axis and the 665 nm peak arising from the longitudinal axis of the structures (37, 44). These results are similar to the absorbance spectrum of one-dimensional plasmonic Au nanorods that possess a similar absorbance quality, observed both experimentally and theoretically (21, 37, 44). Additionally, because the 520 nm peak is consistently positioned, this strongly suggests that growth of the particles occurs in a linear fashion rather than from all three dimensions. Such results are consistent with the end-to-end assembly of Au nanorods, where the transverse plasmon peak remains constant and shifting of the longitudinal peak occurs based upon the assembly mechanism (21, 37, 44). Taken together, the formation of a second absorbance band and the constant position of the 520 nm peak indicate an in-solution linear assembly process, whose results are consistent with the observed linear networks of Au nanoparticles.

An interesting result of this study indicated that the observed assembly process is directly controlled by the concentration of Arg in the solution. To that end, at low Arg concentrations of 40.0 μM (20K sample), the formation of short nanoparticle chains is observed after 6.00 h; however, when compared to the highest concentration of Arg employed in the 100K sample, 200 μM, rapid assembly is noted. This effect is attributed to the on−off equilibrium of the amino acid with the Au nanoparticle surface, which is a direct function of the Arg binding strength. At low Arg concentrations, the equilibrium is shifted toward ligand desorption and results in only small neutralized regions of the amino acid on the nanoparticle surface. As such, the assembly process is slow, thus leading to the minimal degree of assembly observed in the 20K sample. As the Arg concentrations increase to the levels used in the 100K sample, the on−off equilibrium is shifted toward surface adsorption, thus resulting in nanoparticles with a high Arg surface coverage but with a very low surface charge. While this does indeed produce nanoparticle chains and superstructures at short time periods, as depicted in Figure 6a, bulk aggregation of these materials is noted after longer assembly times (>3.00 h by UV−vis). This is due to the fact that the highly branched structures possess very little electrostatic repulsions between nanoparticles, which are required for stability (40), thus generating necks between multiple nanoparticles. As this process ensues, small aggregated regions are observed after 3.00 h (Figure 6b) and eventually the organization mechanism continues over time to form large bulk aggregates, as shown in Figure 6c. These undesirable bulk materials eventually precipitate, which can be avoided by the selection of a lower Arg concentration. While this effect allows for control of the final assembled network, its direct relationship with the side-chain binding strength may be exploited for further comparisons between other amino acids for experimental determination of their intrinsic binding abilities with nanomaterial surfaces.

SUMMARY AND CONCLUSIONS

In summary, we have demonstrated the ability to assemble Au nanoparticles into anisotropic linear assemblies through the specific interactions of the simple amino acid Arg. In this model, Arg is able to displace the citrate surface passivant of 15 nm Au nanoparticles, producing a segregated ligand surface

arrangement. As a result, a patchy charged surface on the Au nanoparticle is achieved, which induces the formation of an electronic dipole across the overall nanoparticle structure. From this dipole, linear assembly of the materials can occur to generate large branched superstructures of the materials in solution. The assembly process is dependent upon the concentration of the amino acid in solution, thus yielding larger assembly rates for higher solution concentrations. These effects are due to two intrinsic factors associated with the ligand/nanoparticle interactions: the actual binding strength of the amino acid and their subsequent arrangement on the nanoparticle surface. These results may represent a way to experimentally compare biomolecular surface binding events using nanomaterials in solution where exploitation of the inherent materials properties can occur rather than by approximations employing two-dimensional surfaces or theoretical calculations. Such a fundamental level of understanding is desirable because biomolecules are becoming increasingly important vehicles for the fabrication of functional nanomaterials. By a comparison of the nanoparticle assembly rates and their final architectures produced, direct information of the binding process from a variety of biomolecules ranging from simple amino acids to complex protein structures may be achievable. Additionally, the unique linearly assembled architectures produced using Arg may be employed for a variety of electronic and optical applications. Further studies on both of these areas are presently underway to address these possibilities.

Acknowledgment. We gratefully acknowledge the University of Kentucky for financial support. The authors also thank the U.K. Microscopy Center and Dr. Alan Dozier for assistance with the TEM analysis. Additionally, we thank Professor Thomas Dziubla from the Department of Chemical and Materials Engineering, University of Kentucky, for assistance with the DLS analysis.

Note Added after ASAP Publication. This article was released ASAP on May 28, 2009, with an author misspelling in ref 24. The correct version was posted on June 10, 2009.

Supporting Information Available: Characterization of the starting materials, TEM analysis of the assembly process over time for all samples, and solvent dielectric effects of materials assembly. This material is available free of charge via the Internet at http://pubs.acs.org.

REFERENCES AND NOTES

(1) Brutchey, R. L.; Morse, D. E. *Chem. Rev.* **2008**, *108*, 4915–4934.
(2) Dickerson, M. B.; Sandhage, K. H.; Naik, R. R. *Chem. Rev.* **2008**, *108*, 4935–4978.
(3) Rosi, N. L.; Mirkin, C. A. *Chem. Rev.* **2005**, *105*, 1547–1562.
(4) Slocik, J. M.; Naik, R. R. *Adv. Mater.* **2006**, *18*, 1988–1992.
(5) Parcardo, D. B.; Sethi, M.; Jones, S. E.; Naik, R. R.; Knecht, M. R. *ACS Nano* **2009**, *3*, 1288–1296.
(6) Slocik, J. M.; Govorov, A. O.; Naik, R. R. *Angew. Chem., Int. Ed.* **2008**, *47*, 5335–5339.
(7) Slocik, J. M.; Zabinsky, J. S.; Phillips, D. M.; Naik, R. R. *Small* **2008**, *4*, 548–551.
(8) Knecht, M. R.; Sethi, M. *Anal. Bioanal. Chem.* **2009**, *394*, 33–46.
(9) Nam, K. T.; Kim, D.-W.; Yoo, P. J.; Chiang, C.-Y.; Meethong, N.; Hammond, P. T.; Chiang, Y.-M.; Belcher, A. M. *Science* **2006**, *312*, 885–888.
(10) Lee, S.-W.; Mao, C.; Flynn, C. E.; Belcher, A. M. *Science* **2002**, *296*, 892–895.
(11) Reiss, B. D.; Mao, C.; Solis, D. J.; Ryan, K. S.; Thomson, T.; Belcher, A. M. *Nano Lett.* **2004**, *4*, 1127–1132.
(12) Naik, R. R.; Stringer, S. J.; Agarwal, G.; Jones, S. E.; Stone, M. O. *Nat. Mater.* **2002**, *1*, 169–172.
(13) Dickerson, M. B.; Jones, S. E.; Cai, Y.; Ahmad, G.; Naik, R. R.; Kröger, N.; Sandhage, K. H. *Chem. Mater.* **2008**, *20*, 1578–1584.
(14) Ahmad, G.; Dickerson, M. B.; Cai, Y.; Jones, S. E.; Ernst, E. M.; Vernon, J. P.; Haluska, M. S.; Fang, Y.; Wang, J.; Subramanyam, G.; Naik, R. R.; Sandhage, K. H. *J. Am. Chem. Soc.* **2008**, *130*, 4–5.
(15) Hnilova, M.; Oren, E. E.; Seker, U. O. S.; Wilson, B. R.; Collino, S.; Evans, J. S.; Tamerler, C.; Sarikaya, M. *Langmuir* **2008**, *24*, 12440–12445.
(16) Hong, G.; Heinz, H.; Naik, R. R.; Farmer, B. L.; Pachter, R. *ACS Appl. Mater. Interfaces* **2009**, *1*, 388–392.
(17) Oren, E. E.; Tamerler, C.; Sarikaya, M. *Nano Lett.* **2005**, *5*, 415–419.
(18) Seker, U. O. S.; Wilson, B.; Dincer, S.; Kim, I. W.; Oren, E. E.; Evans, J. S.; Tamerler, C.; Sarikaya, M. *Langmuir* **2007**, *23*, 7895–7900.
(19) Schravendijk, P.; Ghiringhelli, L. M.; Site, L. D.; van der Vegt, N. F. A. *J. Phys. Chem. C* **2007**, *111*, 2631–2642.
(20) Seker, U. O. S.; Wilson, B.; Sahin, D.; Tamerler, C.; Sarikaya, M. *Biomacromolecules* **2009**, *10*, 250–257.
(21) Sethi, M.; Joung, G.; Knecht, M. R. *Langmuir* **2009**, *25*, 1572–1581.
(22) Willett, R. L.; Baldwin, K. W.; West, K. W.; Pfeiffer, L. N. *Proc. Natl. Acad. Sci. U.S.A.* **2005**, *102*, 7817–7822.
(23) Singh, C.; Ghorai, P. K.; Horsch, M. A.; Jackson, A. M.; Larson, R. G.; Stellacci, F.; Glotzer, S. C. *Phys. Rev. Lett.* **2007**, *99*, 226106.
(24) Uzun, O.; Hu, Y.; Verma, A.; Chen, S.; Centrone, A.; Stellacci, F. *Chem. Commun.* **2008**, 196–198.
(25) Carney, R. P.; DeVries, G. A.; Dubois, C.; Kim, H.; Kim, J. Y.; Singh, C.; Ghorai, P. K.; Tracy, J. B.; Stiles, R. L.; Murray, R. W.; Glotzer, S. C.; Stellacci, F. *J. Am. Chem. Soc.* **2008**, *130*, 798–799.
(26) Jackson, A. M.; Myerson, J. W.; Stellacci, F. *Nat. Mater.* **2004**, *3*, 330–336.
(27) Hu, Y.; Uzun, O.; Dubois, C.; Stellacci, F. *J. Phys. Chem. C* **2008**, *112*, 6279–6284.
(28) Bonell, F.; Sanchot, A.; Dujardin, E.; Péchou, R.; Girard, C.; Li, M.; Mann, S. *J. Chem. Phys.* **2009**, *130*, 034702.
(29) Daniel, M.-C.; Astruc, D. *Chem. Rev.* **2004**, *104*, 293–346.
(30) Lin, S.; Li, M.; Dujardin, E.; Girard, C.; Mann, S. *Adv. Mater.* **2005**, *17*, 2553–2559.
(31) Yoo, E. J.; Li, T.; Park, H. G.; Chang, Y. K. *Ultramicroscopy* **2008**, *108*, 1273–1277.
(32) Brown, S.; Sarikaya, M.; Johnson, E. *J. Mol. Biol.* **2000**, *299*, 725–735.
(33) Sardar, R.; Shumaker-Parry, J. S. *Nano Lett.* **2008**, *8*, 731–736.
(34) Frens, G. *Nat. Phys. Sci.* **1973**, *241*, 20–22.
(35) Lee, J.-S.; Stoeva, S. I.; Mirkin, C. A. *J. Am. Chem. Soc.* **2006**, *128*, 8899–8903.
(36) Thomas, K. G.; Barazzouk, S.; Ipe, B. I.; Joseph, S. T. S.; Kamat, P. V. *J. Phys. Chem. B* **2004**, *108*, 13066–13068.
(37) Sun, Z.; Ni, W.; Yang, Z.; Kou, X.; Li, L.; Wang, J. *Small* **2008**, *4*, 1287–1292.
(38) Chow, M. K.; Zukoski, C. F. *J. Colloid Interface Sci.* **1994**, *165*, 97–109.
(39) Sethi, M.; Joung, G.; Knecht, M. R. *Langmuir* **2009**, *25*, 317–325.
(40) Somasundaran, P.; Markovic, B.; Krishnakumar, S.; Yu, X. In *Handbook of Surface and Colloid Chemistry*; Birdi, K. S., Ed.; CRC Press: New York, 1997.
(41) Zhong, Z.; Subramanian, A. S.; Highfield, J.; Carpenter, K.; Gedanken, A. *Chem.—Eur. J.* **2005**, *11*, 1473–1478.
(42) Zhong, Z.; Patskovskyy, S.; Bouvrette, P.; Luong, J. H. T.; Gedanken, A. *J. Phys. Chem. B* **2004**, *108*, 4046–4052.
(43) Naka, K.; Itoh, H.; Tampo, Y.; Chujo, Y. *Langmuir* **2003**, *19*, 5546–5549.
(44) Jain, P. K.; Eustis, S.; El-Sayed, M. A. *J. Phys. Chem. B* **2006**, *110*, 18243–18253.
(45) Murphy, C. J.; Sau, T. K.; Gole, A. M.; Orendorff, C. J.; Gao, J.; Gou, L.; Hunyadi, S. E.; Li, T. *J. Phys. Chem. B* **2005**, *109*, 13857–13870.
(46) Nikoobakht, B.; El-Sayed, M. A. *Chem. Mater.* **2003**, *15*, 1957–1962.
(47) Sau, T. K.; Murphy, C. J. *Langmuir* **2004**, *20*, 6414–6420.

AM900157M